

LETTERS

NATURE | Vol 439 | 5 January 2006

Vol 439 | 5 January 2006 | doi:10.1038/nature04414

nature

Table 2 | Fits to the occultation chords

Table with 7 columns: Site, P (km), q* (km), Latitudes of suboccultation point (deg.), Radial residual (km) (Circular fit, r = 0 fixed; Elliptical fit, P fixed; Elliptical fit, P free), and Free parameters (Choron's radius, R_c; Offset; Oblateness, epsilon; North pole position angle, P; chi-squared per degree of freedom).

*The timings of Table 1 provide the star position relative to Charon's expected centre, using the DE413/PLU013 Charon ephemeris... The quantity in rounded in the fits is sigma^2 = sum((obs - calc)^2 / (delta t)^2), where delta t_obs, delta t_calc is the distance of the observed (resp. calculated) fit point to the shadow centre, and sigma is the 1-sigma uncertainty in t_obs.

would have important consequences for better constraining not only Pluto's density, but also the Pluto atmosphere models, through a reassessment of occultation observations.

Our data also set an upper limit for a putative atmosphere for Charon. By combining the stellar fluxes observed at the Paranal and El Leoncito observatories, we derive a synthetic light curve, as shown in Fig. 2. The effect of an atmosphere depends on the surface pressure, the nature of the gas and the temperature profile. We assumed two cases. One is that of an isothermal nitrogen (N2) atmosphere at T_s = 56 K, the recently estimated mean dayside Charon surface temperature... The other is a pure methane (CH4) atmosphere, with a temperature increasing from 56 K at the surface to 100 K above 20 km, due to solar heating, as is the case for Pluto's atmosphere... The two cases indicate upper limits of 110 and 15 nbar (3sigma), respectively, with corresponding upper limits of 4.1 and 1.3 cm amagat for the vertical column densities. Limits obtained from the 1980 Charon stellar occultation were about two and ten times larger for N2 and CH4, respectively... Note that in the limiting cases presented here, refraction of stellar rays by the atmosphere would cause a reduction of Charon's shadow radius by about 10 km, when compared to the actual radius, R_c. Consequently, if an atmosphere is detected at those levels in the future, such effects should be considered when deriving R_c.

The very low upper limit for an atmosphere around Charon is not surprising, given estimates of escape rates... The upper limit we derive for a pure methane atmosphere is also consistent with the absence of a CH4 ice signature in its near-infrared spectrum... In fact, a 15 nbar CH4 atmosphere is in equilibrium with CH4 ice at 41 K, much less than the 56 K quoted above. Methane ice could still be present in restricted, colder, regions of the surface. For N2, a 110 nbar atmosphere would imply an even lower equilibrium temperature (T < 31 K), requiring that N2 ice be confined at best to high northern latitudes and/or to permanently shadowed regions of the satellite. The same is true for other candidates, like CO, which would require temperatures as low as 35 K.

Received 2 September; accepted 17 October 2005

1. Christy, J. W. & Harrington, R. S. The satellite of Pluto. Astron. J. 83, 1005-1008 (1978).

2. Olin, C. B., Wasserman, L. H. & Franco, O. G. The mass ratio of Charon to Pluto from Hubble Space telescope astrometry with the fine guidance sensor. Ions 164, 254-259 (2003).
3. Walker, A. R. An occultation by Charon. Mon. Not. R. Astron. Soc. 192, 479-50P (1980).
4. Elliot, J. L. & Young, L. A. Limits on the radius and a possible atmosphere of Charon from its 1993 stellar occultation. Ions 89, 244-254 (1991).
5. Stern, S. A. The Pluto-Charon system. Ann. Rev. Astron. Astrophys. 30, 185-233 (1992).
6. Tholen, D. J. & Buie, M. W. in Pluto and Charon (eds Stern, S. A. & Tholen, D. J.) 193-219 (Univ. Arizona Press, Tucson, 1997).
7. Reinsch, K., Bunz, V. & Festou, M. C. Albedo maps of Pluto and improved physical parameters of the Pluto-Charon system. Ions 108, 209-218 (1994).
8. Tholen, D. J. & Buie, M. W. Further analysis of the Pluto-Charon mutual event observations. Bull. Am. Astron. Soc. 22, 1129 (1990).
9. Buratti, B. J. et al. Modeling Pluto-Charon mutual events. II. CCD observations with the 60 in. telescope at Palomar Mountain. Astron. J. 110, 1405-1409 (1995).
10. Young, E. F. & Bruzel, R. P. A new determination of radii and limb parameters for Pluto and Charon from mutual events. Ions 108, 219-224 (1994).
11. Nutt, G. W. & Owen, W. M. Jr. Charon's Pluto mass ratio obtained with HST CCD observations in 1991 and 1993. Astron. J. 113, 1368-1381 (1996).
12. Tholen, D. J. & Buie, M. W. The orbit of Charon. I. New Hubble Space Telescope observations. Ions 125, 245-260 (1997).
13. Stansberry, J. A., Lunine, J. I., Hubbard, W. B., Yelle, R. V. & Hunter, D. M. Mirages and the nature of Pluto's atmosphere. Ions 111, 503-513 (1994).
14. Yelle, R. V. & Elliot, J. L. in Pluto and Charon (eds Stern, S. A. & Tholen, D. J.) 347-390 (Univ. Arizona Press, Tucson, 1997).
15. McKinnon, W. B., Smollett, S. P. & Schubert, G. in Pluto and Charon (eds Stern, S. A. & Tholen, D. J.) 295-343 (Univ. Arizona Press, Tucson, 1997).
16. Canup, R. M. A giant impact origin of Pluto-Charon. Science 307, 546-550 (2005).
17. Garnwell, M. A. & Butler, B. J. Sub-arcsec scale imaging of the Pluto/Charon binary system at 1.4 microm. Bull. Am. Astron. Soc. 29, 749 (2005).
18. Dumas, C., Tenike, R. J., Brown, R. H., Schneider, G. & Smith, B. A. Hubble Space Telescope NICMOS spectroscopy of Charon's leading and trailing hemispheres. Astron. J. 121, 1163-1170 (2001).

Acknowledgments We thank the Conseil Scientifique of the Paris Observatory and the Programme National de Planéologie for supporting part of the observations of this event in South America.

Author Information Reprints and permissions information is available at www.nature.com/reprints. Correspondence and requests for materials should be addressed to B.S. (bruno.stansberry@obspm.fr).

LETTERS

Structural diversity in binary nanoparticle superlattices

Elena V. Shevchenko^{1,2,†}, Dmitri V. Talapin^{1,†}, Nicholas A. Kotov³, Stephen O'Brien² & Christopher B. Murray¹

Assembly of small building blocks such as atoms, molecules and nanoparticles into macroscopic structures—that is, 'bottom up assembly'—is a theme that runs through chemistry, biology and material science. Bacteria¹, macromolecules² and nanoparticles³ can self-assemble, generating ordered structures with a precision that challenges current lithographic techniques. The assembly of nanoparticles of two different materials into a binary nanoparticle superlattice (BNSL)^{3,7} can provide a general and inexpensive path to a large variety of materials (metamaterials) with precisely controlled chemical composition and tight placement of the components. Maximization of the nanoparticle packing density has been proposed as the driving force for BNSL formation^{3,6,8}, and only a few BNSL structures have been predicted to be thermodynamically stable. Recently, colloidal crystals with micrometre-scale lattice spacings have been grown from oppositely charged poly(methyl methacrylate) spheres^{9,10}. Here we demonstrate formation of more than 15 different BNSL structures, using combinations of semiconducting, metallic and magnetic nanoparticle building blocks. At least ten of these colloidal crystalline structures have not been reported previously. We demonstrate that electrical charges on sterically stabilized nanoparticles determine BNSL stoichiometry; additional contributions from entropic, van der Waals, steric and dipolar forces stabilize the variety of BNSL structures.

Face-centred cubic (f.c.c.) ordering of monodisperse hard spheres dispersed in a liquid permits larger local free space available for each sphere compared to the unstructured phase, resulting in higher translational entropy of the spheres. When the volume fraction of hard spheres approaches ~55%, this ordering enhances the total entropy of the system and drives the ordering phase transition. Entropy-driven crystallization has been studied in great detail both theoretically¹¹ and experimentally on monodisperse latex particles, whose behaviour can be approximated by hard spheres^{12,13}. In a mixture containing spheres of two different sizes (radii R_small and R_large), the packing symmetry depends on the size ratio of the small and large spheres (gamma = R_small/R_large)^{14,8}. Calculations show that assembly of hard spheres into binary superlattices is structurally with NaCl, AlB2 and Na2Zn11 can be driven by entropy alone without any specific energetic interactions between the spheres¹⁵. Indeed, Na2Zn11- and AlB2-type assemblies of silica particles were found in natural Brazilian opals¹⁶ and can be grown from latex spheres¹⁷. In a certain gamma range, the packing density of these structures either exceeds or is very close to the density of the close-packed f.c.c. lattice (0.7405), while structures with lower packing densities are predicted to be unstable^{15,18}.

Despite these predictions, we observed an amazing variety of BNSLs that self-assemble from colloidal solutions of nearly spherical

nanoparticles of different materials (Fig. 1). Coherently packed domains extend up to 10 microm in lateral dimensions, and can display well defined facets (Supplementary Fig. 1). In many cases, several BNSL structures form simultaneously on the same substrate, under identical experimental conditions. The same nanoparticle mixture can assemble into BNSLs with very different stoichiometry and packing symmetry. For example, 11 different BNSL structures were prepared from the same batches of 6.2 nm PbSe and 3.0 nm Pd nanoparticles (Supplementary Fig. 2). We also observe that, in general, BNSLs tolerate much broader gamma ranges than hard spheres: for example, AlB2-type BNSLs assembled from different combinations of PbSe, PbS, Au, Ag, Pd, Fe3O4, CoPt, and Bi nanoparticles in a broad gamma range (Supplementary Fig. 3). Further, we observe BNSLs that could not be identified as isostructural with specific intermetallic compounds (Supplementary Fig. 2). This observed structural diversity of BNSLs defies traditional expectations, and shows the great potential of modular self-assembly at the nanoscale.

The formation of binary structures with packing density significantly lower than the density of single-phase f.c.c. close packing (0.7405) rules out entropy as the main driving force for nanoparticle ordering. Moreover, van der Waals, steric or dipolar interparticle interactions are not sufficient to explain why these low density BNSLs form, instead of their constituents separating into single-component superlattices. Opposite electrical charges on nanoparticles could impart a specific affinity of one type of particle (for example, dodecanethiol-capped Au, Ag, Pd) for another (typically PbSe, PbS, Fe3O4, CoPt, and so on), capped with long chain carboxylic acids). If nanoparticles are oppositely charged, the Coulomb potential would stabilize the BNSL while destabilizing the single-component superlattices. The electrical charges might be present on sterically stabilized nanoparticles even in non-polar solvents¹⁹⁻²¹.

To measure charges on the nanoparticles that form our BNSL, we studied the electrophoretic mobility of PbSe and Au nanocrystals. Laser Doppler velocimetry allows the distribution of electrophoretic mobilities within an ensemble of nanoparticles to be measured. The electrical charge (Z, in units of e) of a spherical particle in a low dielectric solvent in absence of electrolyte can be calculated from the electrophoretic mobility (mu_e) where mu_e = Z/(6*pi*eta*a), eta is the viscosity of the solvent and a is the hydrodynamic diameter of a particle²². With a = 10 nm, we obtain mu_e = 0.27 x 10^-12 cm^2 V^-1 s^-1. These calculated values agree well with the peaks in the experimental mobility distribution for 7.2 nm-diameter PbSe nanocrystals in chloroform (Fig. 2a). Owing to the organic coat (oleic acid), the effective hydrodynamic radius of PbSe nanocrystals extends beyond the crystalline core by 1-2 nm, depending on the density of surface coverage. The peaks in the mobility distribution curve indicate the

¹IBM Research Division, T. J. Watson Research Center, 1101 Kitchawan Road, Yorktown Heights, New York 10598, USA. ²Department of Applied Physics & Applied Mathematics, Columbia University, 200 SW Mudd Building, 500 West 120th Street, New York, New York 10027, USA. ³Department of Chemical Engineering, University of Michigan, Ann Arbor, Michigan 48109, USA. Present address: The Molecular Foundry, Lawrence Berkeley National Laboratory, Berkeley, California 94720, USA. [†]These authors contributed equally to this work.

presence of particles with charges $-e$, 0 , e and $2e$ in a colloidal solution of monodisperse PbSe nanocrystals.

We found that the charges on PbSe nanocrystals can be altered by adding surfactant molecules like carboxylic acids and tri-alkylphosphine oxides. Addition of oleic acid increases the population of positively charged PbSe nanocrystals at the expense of the negatively charged and neutral nanocrystals. Depending on the amount of acid added, the majority of nanocrystals can be adjusted to have either one or two positive charges (Fig. 2b and c). Addition of oleic acid increases the solutions' viscosity, causing the peaks to shift towards lower mobility (compare Fig. 2a-c). The addition of tri-*n*-octylphosphine oxide (TOPO) increases the population of negatively

charged PbSe nanocrystals and reduces the concentration of positively charged nanocrystals (Fig. 2d). Surveys of many samples revealed that the additives reliably shifted the distribution of charge states; however, the initial proportion of particles in each charge state was dependent somewhat on sample processing. Both neutral and negatively charged nanoparticles were detected in chloroform solutions of 4.8 nm dodecanethiol-capped Au nanocrystals (Supplementary Fig. 5). After addition of oleic acid most Au nanoparticles become negatively charged (Fig. 2e), whereas the addition of TOPO neutralizes the Au nanoparticles (Fig. 2f). The charges on PbSe and Au nanoparticles could originate from deviations in nanocrystal stoichiometry and adsorption/desorption of charged capping

ligands. Although these additives are effective in adjusting the particle charge states, the specific interactions by which this charge tuning occurs will require further study (Supplementary Discussion 1).

In the presence of oleic acid, PbSe and Au nanoparticles are oppositely charged (Fig. 2e). The Coulomb potential between two oppositely charged nanoparticles ($Z = \pm 1$) separated by 10 nm of a solvent like chloroform is comparable with kT at room temperature, and solutions of mixed PbSe and metal nanoparticles retain stability for several weeks. The relatively small interparticle potential favours annealing of the BNSLs as they grow. For a NaCl-type BNSL with $Z_A = 1$, $Z_B = -1$ and the nearest-neighbour distance $R_0 = 11.5$ nm (Fig. 1a), the Coulomb binding energy per unit cell is estimated to be $U_{Coul} \approx MZ_A Z_B / (4\pi\epsilon_0\epsilon_r R_0) \approx -0.1$ eV (or about $-4kT$ at the superlattice growth temperature, 50 °C), where $M = -1.7476$ is the Madelung constant. The Coulomb binding energy is comparable to the van der Waals attractive energy expected for a NaCl-type BNSL. The energy of short-range van der Waals forces ($\sim 1/R^6$) can rival long-range Coulomb energy ($\sim 1/R$) only at the nanometre scale. In BNSLs, we can neglect screening of the Coulomb potential by charged species in solution because the Debye screening length ($\sim 10^{-4}$ cm) is much larger than R_0 (refs 10, 11). In an AB₂ BNSL where A and B hold opposite charges, the Coulomb potential per AB₂ 'molecule' is $U_{Coul} \approx -\alpha + \beta_1 Z_A + Z_B^2 N^{2/3}$, where α and β are positive constants and N is the number of assembled nanoparticles (Supplementary Discussion 2).

Coulomb energy determines the stoichiometry of the growing BNSL. An extended three-dimensional BNSL can form only if the positive and negative charges compensate each other. If during growth the BNSL accumulates non-compensated charge, eventually U_{Coul} changes sign from negative to positive and the growth is self-limiting. The superlattice nucleation stage should be less sensitive to the Coulomb interactions. Indeed, we observed that many small domains with different BNSL structures can simultaneously nucleate on the same substrate, but their size does not exceed $\sim 10^2$ nanoparticles. Only one or two structures grow to larger length scales ($\sim 10^4$ – 10^6 particles). BNSLs with many particles per unit cell (for

example, AB₃, AB₂, AB₄, AB₅) might form when both charged and neutral nanoparticles of type B are incorporated into the structures. The presence of differently charged nanoparticles in the colloidal solutions (Fig. 2a and Supplementary Fig. 5) could also contribute to the simultaneous formation of different BNSLs. Intentional addition of a large concentration of charged species into a solution of nanoparticles might reduce the Debye screening length down to R_0 , relaxing the strict rules for BNSL charge neutrality and allowing a range of new structures to be formed¹⁰.

Tuning the charge state of the nanoparticles allows us to direct the self-assembly process. Reproducible switching between different BNSL structures has been achieved by adding small amounts of carboxylic acids, TOPO or dodecylamine to colloidal solutions of PbSe (PbS, Fe₃O₄, and so on) and metal (Au, Ag, Pd) nanocrystals. Figure 3 demonstrates how these additives direct the formation of specific BNSL structures. Combining native solutions of 6.2 nm PbSe and 3.0 nm Pd nanoparticles (particle concentration ratio $\sim 1:5$) results in the formation of several BNSL structures with MgZn₂ and cuboctahedral AB₃ lattices dominating. However, the same nanoparticles assemble into orthorhombic AB- and AB₂-type superlattices after adding oleic acid (Fig. 3a), and into NaZn₁₃- or

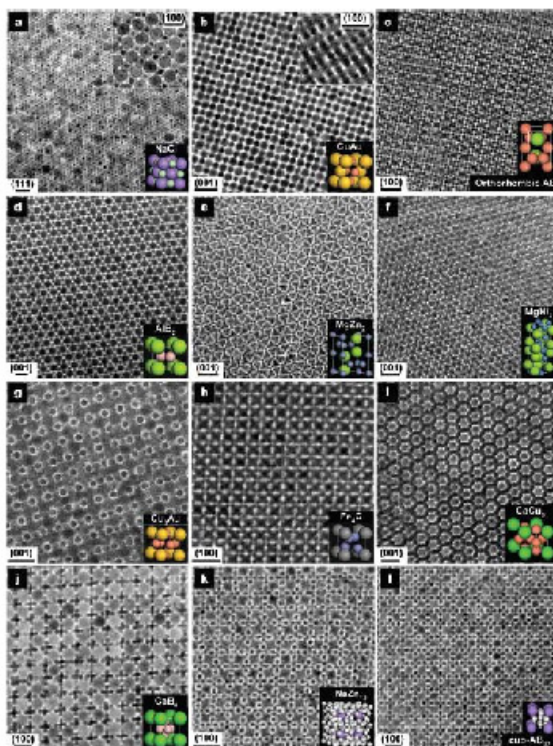


Figure 1 | TEM images of the characteristic projections of the binary superlattices, self-assembled from different nanoparticles, and modelled unit cells of the corresponding three-dimensional structures. The superlattices are assembled from **a**, 13.4 nm γ -Fe₂O₃ and 5.0 nm Au; **b**, 7.6 nm PbSe and 4.9 nm Au; **c**, 6.2 nm PbSe and 3.0 nm Pd; **d**, 6.7 nm PbS and 5.0 nm Pd; **e**, 6.2 nm PbSe and 3.0 nm Pd; **f**, 5.8 nm PbSe and 3.0 nm Pd; **g**, 7.2 nm PbSe and 4.2 nm Ag; **h**, 6.2 nm PbSe and 3.0 nm Pd; **i**, 7.2 nm PbSe and 5.0 nm Au; **j**, 5.8 nm PbSe and 3.0 nm Pd; **k**, 7.2 nm PbSe and 4.2 nm Ag; **l**, 6.2 nm PbSe and 3.0 nm Pd nanoparticles. Scale bars: **a**–**c**, **e**, **f**, **i**–**l**, 20 nm; **d**, **g**, **h**, 10 nm. The lattice projection is labelled in each panel above the scale bar. The modelled projections of the binary superlattices are shown in Supplementary Fig. 4.

Figure 2 | Electrophoretic mobility of PbSe and Au nanocrystals in chloroform. **a**–**d**, Distribution of electrophoretic mobility for 7.2 nm PbSe nanocrystals. **a**, PbSe nanocrystals washed to remove excess of capping ligands. The grey bars show mobilities predicted for nanocrystals with charges of -1 , 0 , 1 and 2 (in units of e). **b**–**d**, Electrophoretic mobility of PbSe nanocrystals in the presence of **b**, 0.02 M oleic acid; **c**, 0.06 M oleic acid and **d**, 0.05 M tri-*n*-octylphosphine oxide. **e**, **f**, Comparison of electrophoretic mobilities of 7.2 nm PbSe and 4.8 nm Au nanocrystals in the presence of **e**, 0.02 M oleic acid and **f**, 0.05 M tri-*n*-octylphosphine oxide, respectively. a.u., arbitrary units.

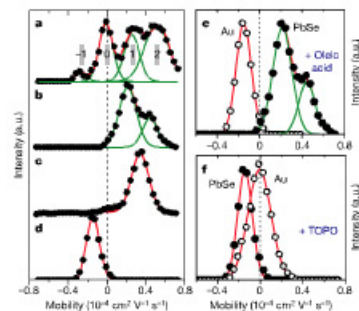


Figure 3 | TEM images of binary superlattices self-assembled in the presence of 4 mM oleic acid (left column) and 6 mM tri-*n*-octylphosphine oxide, TOPO (right column). **a**, 6.2 nm PbSe and 3.0 nm Pd nanoparticles self-assembled into orthorhombic AB- and AB₂-type BNSLs, and **b**, into NaZn₁₃-type BNSL. **c**, **d**, 7.2 nm PbSe and 4.2 nm Ag nanoparticles self-assembled into orthorhombic AB and cuboctahedral AB₃ BNSLs, respectively. **e**, **f**, 6.2 nm PbSe and 5.0 nm Au nanoparticles self-assembled into CuAu-type and CuAu₂-type BNSLs, respectively.

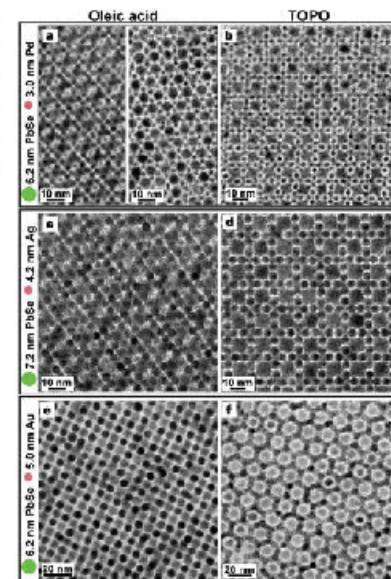


Figure 3 | TEM images of binary superlattices self-assembled in the presence of 4 mM oleic acid (left column) and 6 mM tri-*n*-octylphosphine oxide, TOPO (right column). **a**, 6.2 nm PbSe and 3.0 nm Pd nanoparticles self-assembled into orthorhombic AB- and AB₂-type BNSLs, and **b**, into NaZn₁₃-type BNSL. **c**, **d**, 7.2 nm PbSe and 4.2 nm Ag nanoparticles self-assembled into orthorhombic AB and cuboctahedral AB₃ BNSLs, respectively. **e**, **f**, 6.2 nm PbSe and 5.0 nm Au nanoparticles self-assembled into CuAu-type and CuAu₂-type BNSLs, respectively.

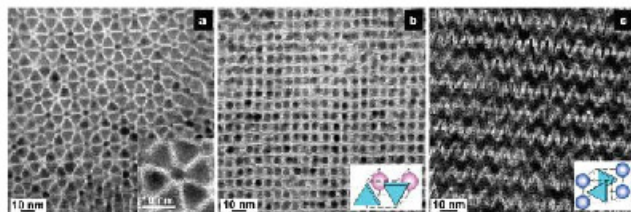


Figure 4 | TEM images and proposed unit cells of binary superlattices self-assembled from triangular nanoplates and spherical nanoparticles. a, b, Self-assembled from LaF₃ triangular nanoplates (9.0 nm side) and 5.0 nm Au nanoparticles; c, self-assembled from LaF₃ triangular nanoplates

and 6.2 nm PbSe nanoparticles. The insets show a, a magnified image, and b, c, proposed unit cells of the corresponding superlattices. The structure shown in a forms on silicon oxide surfaces, while structures shown in b and c form preferentially on amorphous carbon substrates.

cuboctahedral AB₁₃-type BNSIs after the addition of dodecylamine or TOPO, respectively (Fig. 3b). In the AB₁₃-type BNSI, metal particles assemble into icosahedral (Au₁₃Zn₁₃) or cuboctahedral (cuboctahedral AB₁₃) clusters, with each large PbSe particle surrounded by 24 metal spheres at the vertices of a snub cube²¹. In the presence of TOPO the metal nanoparticles are neutral (Fig. 2f), favouring formation of the Pd₁₃(Au₁₃, Ag₁₃) clusters. The clusters of metal nanoparticles in turn provide screening of the charges on PbSe nanocrystals in the AB₁₃-type BNSI.

Surveys of many samples show that the addition of a carboxylic acid to solutions of PbSe-Pd, PbSe-Au, PbSe-Ag and PbSe-Fe₃O₄ nanoparticle mixtures results in either AB or AB₁₃ superlattices (Fig. 3c, e), whereas the addition of TOPO to mixtures of the same nanoparticles favours growth of AB₁₃ (if $\gamma < -0.65$) or AB₁ (if $\gamma > -0.65$) BNSIs (Fig. 3d, f). Thus the space-filling principles and particle charging work in combination to determine the structure. Adjusting the relative concentrations of A and B particles can be used as an additional tool with which to control the BNSI structure. For example, in presence of TOPO, AB₁₃ BNSIs can form when the AB ratio is -1.1 , whereas exclusively AB₁₃ forms in the presence of large excess B particles.

In contrast to particles with amorphous or polycrystalline morphology, nanocrystals allow exploitation of the inherent crystal anisotropy to precisely engineer nanocrystal shape²². The nanocrystal shape can in turn be used as a powerful tool to engineer the structure of the self-assembled BNSIs. For example, Fig. 4 shows several BNSIs self-assembled from LaF₃ triangular nanoplates and spherical Au or PbSe nanocrystals. In the LaF₃-Au system, the LaF₃ nanoplates lie flat on silicon oxide surface (Fig. 4a) and stand on edge when assembled on amorphous carbon (Fig. 4b and c), demonstrating how the choice of substrate can be used to control the BNSI structure.

It is specifically at the nanoscale that the van der Waals, electrostatic, steric repulsion and the directional dipolar interactions can contribute to the interparticle potential with comparable weight^{23,24}. These, together with the effects of particle substrate interactions and space-filling (entropic) factors, combine to determine the BNSI structure. The non-equilibrium nature of our evaporative self-assembly process adds additional complexity²⁵. Precise control of nanoparticle size, shape and composition allows us to engineer electronic, optical and magnetic properties of nanoparticle building blocks. Assembling these nanoscale building blocks into a wide range of BNSI systems provides a powerful modular approach to the design of 'metamaterials' with programmable physical and chemical properties.

METHODS

Nanoparticle synthesis. Au, Ag and Pd nanoparticles were prepared by modifying the method of ref. 27. Metal salts were dissolved in 10 ml of toluene, with ultrasonication in the presence of dodecyltrimethylammonium bromide

(DDAAB). For synthesis of 5.0 nm Au and 4.2 nm Ag nanoparticles, we used 0.044 g AuCl₃ and 0.025 g AgNO₃, respectively, and 0.0925 g DDAAB, 3.0 mm Pd nanocrystals were synthesized from 0.037 g PdCl₂ with 0.037 g DDAAB. Forty microlitres of a 9.4 M aqueous solution of NaBH₄ were added drop-wise to the solution of metal salt with vigorous stirring. After 20 min, 0.8 ml 1-dodecanol was added and the stirring was continued for five more minutes. The nanoparticles were precipitated by adding ethanol, and the solid redispersed in 10 ml toluene in the presence of 0.8 ml 1-dodecanol and refluxed for 30 min under nitrogen. Fe₃O₄ nanocrystals were synthesized by methods adapted from ref. 28. Briefly, 11 mm and 13.4 mm Fe₂O₃ nanocrystals were synthesized by injecting 0.2 ml iron pentacarbonyl into 10 ml trimethylamine in the presence of 0.65 g oleic acid at 270 °C and 250 °C, respectively. After heating of the reaction mixtures at 320 °C for 1 h, the reaction mixture was cooled to room temperature. 0.17 g trimethylamine-N-oxide was added to oxidize the iron nanoparticles to γ -Fe₂O₃ and the reaction mixture was heated to 180 °C for 1.5 h and 320 °C for 1 h. Details of the synthesis of PbSe, PbS and LaF₃ nanocrystals can be found in refs 7, 29 and 30, respectively.

Preparation of binary superlattices. A substrate for example, a carbon- or silicon oxide-coated transmission electron microscope (TEM) grid, a silicon nitride membrane or an allyl-functionalized silicon chip) was placed in a glass vial containing a colloidal solution of nanoparticles. The vial was placed tilted by 60°–70° inside a low-pressure chamber. Ordered binary assemblies formed upon evaporation of the solvent. Toluene and mixtures of toluene with tetrahydrofuran or chloroform were used as solvents (1–1) by volume. The best binary assemblies (as determined by the length scale of ordering and a low occurrence of defects) were obtained by evaporating relatively concentrated colloidal solutions at 45 °C under reduced pressure (-3.2 kPa).

Structural analysis. A Philips CM12 TEM operating at 120 kV was used to image the structure of the assemblies. Three-dimensional descriptions of the superlattices were developed by surveying large regions of the samples, to categorize all the crystal orientations, and recording a series of two-dimensional projections down the major symmetry axes. Tilted of the samples allowed observation of additional orientations not expressed in the plan view images. To assign the observed structures to crystallographic space groups, we built three-dimensional lattice models for the 180 most common space groups using Accelrys MS Modelling 3.1 software. The TEM images were compared with simulated projections to match the symmetry of our superlattices. We also performed a comparison of experimental small-angle electron diffraction patterns taken over larger areas, and the two-dimensional Fourier transformation power spectra of real space TEM images and the fast Fourier transform power spectra of the simulated projections to assure consistency.

Electrophoretic mobility measurements. These were performed by electrophoretic light scattering using a Zetasizer Nano ZS Series (Malvern), allowing measurements in non-polar organic solvents. We used chloroform solutions with nanoparticle concentrations ~ 3 times higher than those used for growing binary superlattices. The concentrations of additives (oleic acid and TOPO) were similar to those used for directing BNSI self-assembly. After preparation, the colloidal solutions were left in the dark for several hours to allow the systems to equilibrate before each measurement.

Received 20 August; accepted 2 November 2005.

1. Shenton, W., Purn, D., Sleytr, U. & Mann, S. Synthesis of cadmium sulphide superlattices using self-assembled bacterial S-layers. *Nature* **399**, 585–587 (1997).

2. Guarni, K. W., Block, C. T. & Yeung, S. H. I. Optimization of diblock copolymer thin film self assembly. *Adv. Mater.* **14**, 1290–1294 (2002).
3. Redl, F. X., Cho, K.-S., Murray, C. B. & O'Brien, S. Three-dimensional binary superlattices of magnetic nanocrystals and semiconductor quantum dots. *Nature* **423**, 968–971 (2003).
4. Kely, C. J., Fink, J., Brust, M., Bethel, D. & Schlöf, D. J. Spontaneous ordering of bimodal ensembles of nanoscopic gold clusters. *Nature* **396**, 444–446 (1998).
5. Shevchenko, E. V. et al. Colloidal synthesis and self-assembly of CoPt₂ nanocrystals. *J. Am. Chem. Soc.* **124**, 11480–11485 (2002).
6. Saunders, A. E. & Korgel, B. A. Observation of an AB phase in bidisperse nanocrystal superlattices. *ChemPhysChem* **6**, 61–65 (2005).
7. Shevchenko, E. V., Talapin, D. V., O'Brien, S. & Murray, C. B. Polymorphism in AB₁₃ nanoparticle superlattices: An example of semiconductor-metal metamaterials. *J. Am. Chem. Soc.* **127**, 8741–8747 (2005).
8. Murray, M. J. & Sanders, J. V. Close-packed structures of spheres of two different sizes. II. The packing densities of likely arrangements. *Phil. Mag.* **A42**, 721–740 (1980).
9. Eldridge, M. D., Madden, P. A. & Frenkel, D. Entropy-driven formation of a superlattice in a hard-sphere binary mixture. *Nature* **365**, 35–37 (1993).
10. Leuninger, M. E. et al. Ionic colloidal crystals of oppositely charged particles. *Nature* **437**, 235–240 (2005).
11. Bartlett, P. & Campbell, A. I. Three-dimensional binary superlattices of oppositely charged colloids. *Phys. Rev. Lett.* **95**, 128302 (2005).
12. Bolhuis, P. G., Frenkel, D., Mau, S.-C. & Huse, D. A. Entropy difference between the face-centred cubic and hexagonal close-packed crystal structures. *Nature* **388**, 235–236 (1997).
13. Pusey, P. N. & van Meegen, W. Phase behaviour of concentrated suspensions of nearly hard colloidal spheres. *Nature* **320**, 340–342 (1986).
14. Wang, S., Klauwa, V. & Oam, G. A. Colloidal crystal films. *Advances in universality and perfection*. *J. Am. Chem. Soc.* **125**, 15589–15598 (2003).
15. Gollin, X. & Monson, P. A. Substitutionally ordered solid solutions of hard spheres. *J. Chem. Phys.* **102**, 3354–3360 (1995).
16. Sanders, J. V. & Murray, M. J. Ordered arrangements of spheres of two different sizes in opal. *Nature* **275**, 201–203 (1978).
17. Hachisu, S. & Yoshimura, S. Optical demonstration of crystalline superlattices in binary mixtures of latex globules. *Nature* **283**, 188–189 (1980).
18. Shim, M. & Guyot-Sionnest, P. Permanent dipole moment and charges in colloidal semiconductor quantum dots. *J. Chem. Phys.* **111**, 6955–6964 (1999).
19. Krauss, T. D. & Bus, L. E. Charge, polarizability, and photoionization of single semiconductor nanocrystals. *Phys. Rev. Lett.* **83**, 4840–4843 (1999).
20. Islam, M. A. & Herman, I. P. Electrodeposition of patterned CdSe nanocrystal films using thermally charged nanocrystals. *Appl. Phys. Lett.* **80**, 3823–3825 (2002).
21. O'Brien, R. W. & White, L. R. Electrokinetic mobility of a spherical colloidal particle. *J. Chem. Soc. Farad. Trans. 2* **74**, 1607–1626 (1978).

Supplementary Information is linked to the online version of the paper at www.nature.com/nature.

Acknowledgements We thank V. Perebenko, A. van Blaaderen, V. Crespi, I. Herman and L. E. Bus for discussions and R. L. Sandstrom for technical support. This work was partially supported by the MRSEC Program of the National Science Foundation, and by the New York State Office of Science, Technology and Academic Research (NYSTAR). S.O. is grateful for support from the DOE and an NSF CAREER award.

Author Contributions E.V.S. and D.V.T. contributed equally to this work. E.V.S. and D.V.T. carried out synthesis of nanoparticles, and E.V.S. investigated formation of binary nanoparticle superlattices. E.V.S. and D.V.T. performed modelling and structural assignment of self-assembled binary superlattices. E.V.S., D.V.T. and N.A.K. studied electrophoretic mobility of nanoparticles and worked on modelling self-assembly phenomena in binary nanoparticle colloids. S.O. and C.B.M. initiated and supervised the work. D.V.T. and C.B.M. wrote the paper. All authors discussed the results and commented on the manuscript.

Author Information Reprints and permissions information is available at www.nature.com/reprints/permissions. The authors declare no competing financial interests. Correspondence and requests for materials should be addressed to D.V.T. (dvtalpin@illinois.gov) or C.B.M. (cbmurray@us.ibm.com).